Density-stable displacement flow of immiscible fluids in inclined pipes

Olamide Oladosu,[1] Aqib Hasnain,[2] Paris Brown,[1] Ian Frigaard,[3] and Kamran Alba[1,*]

[1]*Department of Engineering Technology, University of Houston, 304 Technology Building 2, Houston, Texas 77204, USA*

[2]*Department of Mechanical Engineering, University of California, Santa Barbara, California 93106, USA*

[3]*Department of Mathematics and Department of Mechanical Engineering, University of British Columbia, 1984 Mathematics Road, Vancouver, British Columbia V6T 1Z2, Canada*

(Received 8 November 2018; published 24 April 2019)

We study experimentally the isoviscous displacement flow of two immiscible Newtonian fluids in an inclined pipe. The less dense displacing fluid is placed above the denser displaced fluid in a density-stable configuration. The displacing and displaced solutions are oil- and water-based, respectively. The former exhibits nonwetting behavior in the vicinity of the pipe wall, whereas the latter is wetting. The pipe has a small diameter-to-length ratio. The mixing and interpenetration of two fluids have been studied over a wide range of controlling parameters, revealing remarkable results. Compared to the previously studied miscible limit, we observe behavior at the interface between the two fluids where the displaced fluid stays "pinned" to the lower wall of the pipe upon pumping the displacing one. This phenomenon, which is observed over the full range of investigated flow rates, tilt angles, and density contrasts, is associated with the wetting characteristic of the displacing liquid and is also present when light and heavy viscosity mineral oils are used as the displacing fluid. Ultrasonic Doppler velocimetry revealed a segmented velocity profile at the interface of the immiscible fluids. Due to pinning, the efficiency of the removal of displaced fluid in the immiscible limit can be lowered by 14% compared to the miscible case due to the combined effects of the density-stable configuration and the immiscibility of the flow. Within the family of immiscible fluids, the maximum efficiency is achieved at close-to-vertical tilt angles, large density contrasts, and counterintuitively low imposed flow rates, which is of great importance in industrial design.

DOI: 10.1103/PhysRevFluids.4.044007

I. INTRODUCTION

Displacement flows, or removal of one fluid by another, are common in a wide range of industries, including food processing [1], water treatment [2], and oil and gas [3]. The last has significantly motivated the present study. During the cementing phase of a conventional oil and gas well, a series of water-based fluids are often pumped into the wellbore, which can be at diverse tilt angles from the vertical direction [3]. However, for deep water and unconventional shale wells, high-performance oil-based fluids can instead be used in order to reduce drilling risks [4,5]. Existence of both water- and oil-based phases during removal or cleaning operations introduces immiscibility effects, which in turn can significantly increase the complexity of the problem.

Previous studies have examined buoyancy-driven miscible flows experimentally [6] and theoretically [7] in a lock-exchange configuration (no imposed flow), focusing on the effects of pipe inclination and density contrast. Miscible flows with nonzero imposed velocity have also been

*Corresponding author: kalba@central.uh.edu

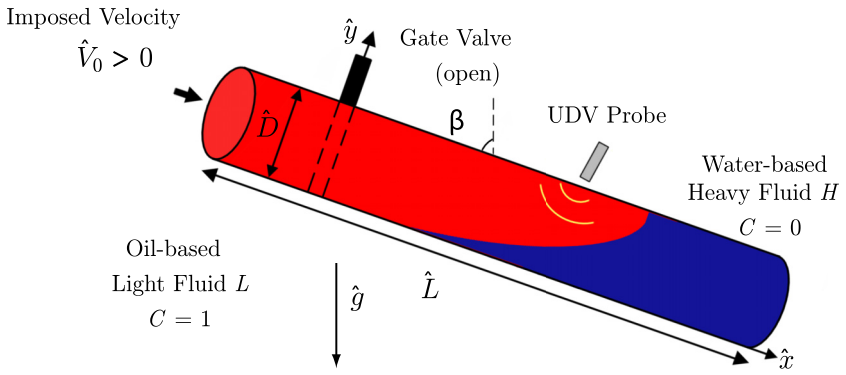

FIG. 1. Schematic view of the experimental setup used. Interface shape is illustrative only.

studied through experimental and theoretical approaches, revealing novel laminar and turbulent flow regimes [8,9]. Different geometries have been employed in miscible studies, including capillary tubes [10], pipes [11], and Hele-Shaw cells [12], revealing sinuous and finger instabilities due to different viscosities of the displacing and displaced fluids. Both water-based [14] and oil-based fluid pairs [13] have been studied under miscibility as well. Immiscible flows have not been studied to as great an extent, contributing to the impetus for this work. Hasnain *et al.* [15] studied immiscible displacement flows in a density-unstable configuration (heavy displacing light) over a range of pipe inclination angles, density differences, and flow rates.

This study is a sequel to two major studies in the literature: Alba *et al.* [16] and Hasnain *et al.* [15]. The former considers a *density-stable* configuration for *miscible* fluids, whereas the latter explores a *density-unstable* configuration in the *immiscible* limit. Alba *et al.* [16] found that after an initial transient period, the interface between miscible fluids settled into a constant shape. The distance between subsequent identical shapes, defined as the fully developed stretch length $\hat{L}$, increased in a more horizontal pipe and decreased with a larger density difference. Miscible fluids were found to have a displacement efficiency of about 96%. Hasnain *et al.* [15] found that immiscible fluids in a density-unstable configuration were characterized by instabilities due to surface tension and shearing effects. Viscous, transition (partially viscous and partially dispersed), and dispersed regimes were observed, in which the shape of the flow interface becomes progressively more unstable, moving from slumped flow that preserved distinct regions of both fluids to droplet formation, where both water-in-oil (w/o) and oil-in-water (o/w) dispersions were observed.

The significant contribution of our study is to combine *density-stable* and *immiscible* flow effects, which has not been carried out before in the literature to the best of our knowledge. Our study covers a wide range of flow rates and pipe inclination angles. We discuss the experimental setup in the following section and then present the main features of immiscible density-stable flows, characterized with relevant dimensionless parameters. We also present the effects of parameteric variations on displacement efficiency, with a brief summary provided towards the end.

II. EXPERIMENTAL SETUP

A. Apparatus and measurement

Our experiments have been conducted in a 2-m-long acrylic pipe of inner diameter $\hat{D} = 9.53$ mm, the same as the one used in our recent experimental study [15]; see Fig. 1 for a schematic representation. Briefly, the pipe can be tilted to any angle β between vertical ($\beta = 0^\circ$) and horizontal ($\beta = 90^\circ$) states. An initially closed, pneumatically actuated gate valve (operated at 103 kPa), located 40 cm from the upper end of the setup, separates the pipe into two sections. Flow into

TABLE I. Parameter range of our experimental study.

Parameter	Name	Range
$\hat{V}_0$	Mean imposed velocity	69–1054 (mm s^{-1})
$\hat{\mu}$	Viscosity	0.005, 0.018, 0.129 (Pa s)
$\hat{\sigma}$	Surface tension	3.5, 10.1, 33.4 (mN m^{-1})
β	Inclination angle	0, 15, 30, 45, 60, 75, 85 (deg)
θ	Fluids contact angle	52, 56, 59 (deg)
$\mathrm{At} = (\hat{\rho}_L - \hat{\rho}_H)/(\hat{\rho}_L + \hat{\rho}_H)$	Atwood number (measure of density difference)	−0.042, −0.075, −0.125
$\mathrm{Re} = \hat{V}_0\hat{D}/\hat{\nu}$	Reynolds number (Inertial to viscous stress)	6–1992
$\mathrm{Fr} = \hat{V}_0/\sqrt{\mathrm{At}\hat{g}\hat{D}}$	Densimetric Froude number (inertial to buoyant stress)	1–17
$\mathrm{Ca} = \hat{\mu}\hat{V}_0/\hat{\sigma}$	Capillary number (viscous to surface tension stress)	0.10–1.51

the pipe is steady and gravity-driven, achieved by an elevated displacing fluid tank in the laboratory. Experiments are conducted mainly in the laminar regime; see Table I for the full parameter range of this study. Throughout this paper, dimensional parameters are denoted with a "hat" (ˆ) symbol and dimensionless parameters without.

The density of the light fluid is denoted by $\hat{\rho}_L$ and that of the heavy fluid by $\hat{\rho}_H$. The displaced fluid in the experiments is water densified by calcium chloride ($CaCl_2$) in the range of 0–290 g $liter^{-1}$, resulting in a density of $\hat{\rho}_H \in [997, 1181]$ kg m^{-3}. Black dye (ink) with a concentration of 800 mg $liter^{-1}$ is added to the displaced fluid in order to measure concentration via optical absorption [17]. The low concentration of dye used does not change the fluid properties. The less dense displacing fluid, on the other hand, is an oil, in most experiments, silicone oil of density $\hat{\rho}_L = 918\,\mathrm{kg\,m^{-3}}$ and viscosity $\hat{\mu}_L = 0.005\,\mathrm{Pa\,s}$.

In this study, refractive indices were not matched between themselves and the material of the tube. However, the refractive index of fluids used is close to that of acrylic, i.e., $n \approx 1.33$, 1.40, and 1.49 for water, silicone oil, and acrylic, respectively, which further reduces light refraction errors. In areas where the pipe refraction gave rise to known errors, as in the case of images generated using ultrasonic Doppler velocimetry (UDV), the error is acknowledged and guides are provided, as in Fig. 11 below. The use of a *fish tank* may reduce refraction errors associated with the curvature of the pipe [18,19]. While it is possible that the reported profiles of interface and displaced residual fluid layer slightly change via the use of a fish tank, recent benchmarking studies have shown that refraction errors do not affect bulk behavior of the flow and most importantly the displacing front velocity [15,20,21].

As our focus is on isoviscous experiments, a small amount of xanthan gum thickener (245 mg $liter^{-1}$ mixed for 20 min at 400 rpm using an IKA F2M03GLA mixer) is added to the saltwater solution to match the viscosity of silicone oil. Upon rheological characterization using a HR-3 Discovery Hybrid Rheometer from TA Instruments, it was found that the shear-thinning effects associated with xanthan gum for the concentration given and our range of shear rate ($\hat{\dot{\gamma}} \in [0, 100]\,\mathrm{s^{-1}}$) are negligible ($\hat{\mu}_H \approx 0.004$–$0.006$ Pa s). Accordingly, the viscosities of the light and heavy fluids are assumed to be equal ($\hat{\mu}_H \approx \hat{\mu}_L \approx \hat{\mu}$).

To measure the axial velocity profile of the flow, an ultrasonic Doppler velocimeter (model DOP400, Signal Processing SA) was mounted 950 mm downstream of the gate valve at an angle of ≈75° from the pipe axis. The UDV probe measures the speed of a flow using the reflection of sound waves from particles within the flow, and the chosen angle balances a good signal to noise ratio with reflections from the pipe wall [22]. Polyamide seeding particles (PSPs) with a diameter

of 50 μm were used as the fluid tracer, selected for their density, which is close to that of the fluids ($\hat{\rho}_{psp} = 1030$ kg m^{-3}) in order to keep them neutrally buoyant in the flow. A PSP concentration of 0.5 g liter^{-1} in both fluids ensured an acceptable UDV echo, and a 4-MHz transducer was used to take the measurements. The surface tension between the fluids was measured with a Sigma 701 Force Tensiometer (Biolin Scientific Inc.). The device has been successfully calibrated against air-water ($\hat{\sigma} = 72.9$ mN m^{-1}) and air-silicone oil ($\hat{\sigma} = 22.1$ mN m^{-1}) [15].

At the start of each experiment, the gate valve is opened, and the flow moves under the influence of gravity towards the drain. The volumetric flow rate, $\hat{Q} = \pi \hat{D}^2 \hat{V}_0/4$, is controlled by the adjustment of a needle valve located before the drain and is measured using a beaker and a stopwatch. This method, which is accurately calibrated in our test experiments, showed superiority over rotameter and magnetic flow meter measurements due to existence of oil and water mixtures with nonstandard viscosity ($\hat{\mu} \neq 0.001$ Pa s). Here $\hat{V}_0$ is the mean imposed velocity. The experiment is captured using a high-speed black-and-white digital camera (Basler Ace acA2040-90um CMOS, 2048^2 pixels) with 4096 gray-scale levels that facilitate analysis of a wide range of concentrations. The camera captures the entire 2-m length of the pipe within its field of view using a high-resolution lens (16 mm F/1.8. C-mount) and records images at a rate of 12–71 Hz, as a function of the imposed flow rate. A well-tested MATLAB image processing code is used to convert gray-scale images from the camera into color pictures for presentation and analysis purposes [15,16].

B. Cleaning procedure using soap water

Prior to each experiment, the pipe is filled above the gate valve with the displacing fluid and below the gate valve with the displaced fluid. During the experiment, the oil-based displacing fluid fills the length of the pipe, flushing out the water-based displaced fluid. At the time of the next experiment, a thin layer of oil can still remain in the bottom portion of the pipe below the gate valve, which can introduce an error into our study. A meticulous cleaning procedure involving soap-water is therefore employed to remove this unwanted layer of oil. This would ensure that the oil-based solution does not contaminate the water introduced into the lower portion of the pipe for the next experiment set. Liquid soap is added to water at a concentration of 1.9 g liter^{-1}. This solution is mixed (3 s at 5 rpm) and then pumped through the pipe for 3 s at high velocity. The pipe is allowed to empty, and then the process is repeated, with soapy water pumped for 3 s once more. The pipe is again drained, and subsequently water is pumped through the pipe at a high velocity for 10 s to flush all the *in situ* fluids out. The authors recognize that the soap can possibly introduce small quantities of residual surfactant molecules into the pipe. In order to minimize the effect of any such molecules introduced into the pipe by the soap, the pipe is drained one last time, and water is pumped through at high velocity once more for 10 s in order to ensure a clean, oil-free pipe. This cleaning procedure is employed for each experiment (total of 120). Note that due to the special configuration of water and oil-based fluids in pipe in the experimental study of Hasnain *et al.* [15], such a soap-water cleaning procedure was not required.

C. Parameter range

An analysis of the flows in this study reveals several relevant dimensional and dimensionless paramters. The pipe inclination angle, β, ranges from vertical ($\beta = 0^\circ$) to near-horizontal ($\beta = 85^\circ$). Experiments are conducted in the $\delta \ll 1$ range, where $\delta = \hat{D}/\hat{L}$ represents the aspect ratio of the pipe. The Atwood number, $\mathrm{At} = (\hat{\rho}_L - \hat{\rho}_H)/(\hat{\rho}_L + \hat{\rho}_H)$, is a measure of density difference of the light and heavy fluids. For this study, $\mathrm{At} < 0$, as we focus on the density-stable configuration [16]. Due to the magnitude of At in our study, both Boussinesq and weakly non-Boussinesq effects may be relevant [15]. The fourth parameter is the Reynolds number, defined as $\mathrm{Re} = \hat{V}_0 \hat{D}/\hat{\nu}$, where $\hat{\nu}$ incorporates the average density of the fluids [$\hat{\rho} = (\hat{\rho}_L + \hat{\rho}_H)/2$] and the viscosity $\hat{\mu}$ that is common to both fluids. The densimetric Froude number, $\mathrm{Fr} = \hat{V}_0/\sqrt{\mathrm{At}\hat{g}\hat{D}}$, captures the relationship between inertial and buoyancy forces, while the relevance of the capillary number, $\mathrm{Ca} = \hat{\mu}\hat{V}_0/\hat{\sigma}$,

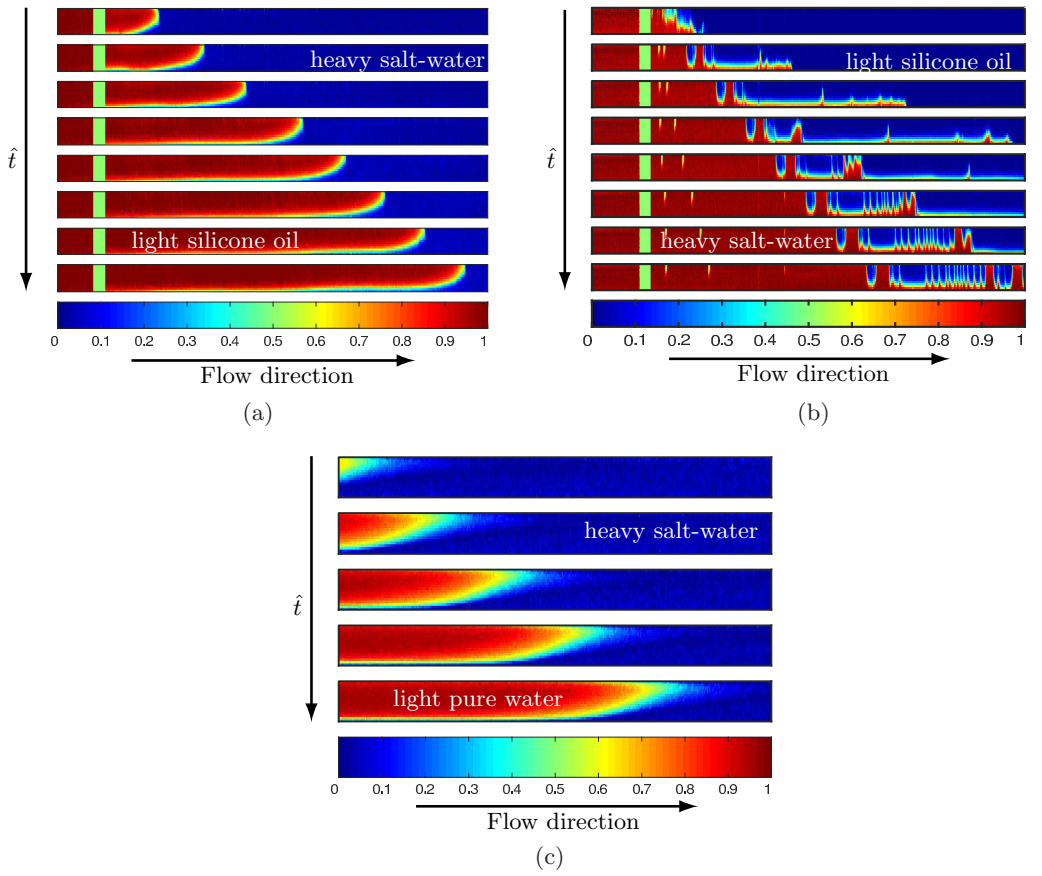

FIG. 2. (a) Immiscible density-stable, (b) immiscible density-unstable, and (c) miscible density-stable displacements. The bottommost image in each panel is a color bar of concentration C, with 0 and 1 referring to the displaced and displacing fluids, respectively. For comparison, panels (a) and (c) are of similar Reynolds number. (a) Snapshots of the displacement flow for $\beta = 45°$, $\hat{V}_0 = 456.9\,\text{mm s}^{-1}$, $\hat{\rho}_H = 1181\,\text{kg m}^{-3}$, and $\hat{\rho}_L = 918\,\text{kg m}^{-3}$, at times $\hat{t} = [0.42,\ 0.84,\ 1.26,...,\ 2.94,\ 3.36]$ s (At $= -0.125$, Re $= 914$, Fr $= 4.22$, Ca $= 0.65$, $\theta = 56°$). The field of view is $1732 \times 9.53\,\text{mm}^2$. (b) Snapshots of the displacement flow for $\beta = 60°$, $\hat{V}_0 = 81.4\,\text{mm s}^{-1}$, $\hat{\rho}_H = 1181\,\text{kg m}^{-3}$, and $\hat{\rho}_L = 918\,\text{kg m}^{-3}$, at times $\hat{t}$=[0.41, 3.39, 6.38,..., 18.27, 21.25] s (At $= 0.125$, Re $= 163$, Fr $= 0.75$, Ca $= 0.12$, $\theta = 56°$). The field of view is $1950 \times 9.53\,\text{mm}^2$. (Figure taken from Hasnain *et al.* [15].) (c) Snapshots of the displacement flow for $\beta = 70°$, $\hat{V}_0 = 20.9\,\text{mm s}^{-1}$, $\hat{\rho}_H = 1007\,\text{kg m}^{-3}$, and $\hat{\rho}_L = 999\,\text{kg m}^{-3}$, at times $\hat{t} = [21.5,\ 24.75,\ 28.00,...,\ 34.50]$ s (At $= -0.0035$, Re $= 855.2$, Fr $= 0.82$). The field of view is $430 \times 19\,\text{mm}^2$, taken 800 mm below the gate valve. (Figure taken from Alba *et al.* [16].)

and fluids contact angle, θ, arises from the immiscibility considered in the flow [15]. The range of these dimensionless parameters is shown in Table I. Both dimensional and dimensionless quantities are provided in figure captions for convenience.

III. RESULTS

A. Flow characterization

First, we present the main features of immiscible density-stable displacement flows. Figure 2 shows a typical experiment in which silicone oil displaces densified $CaCl_2$-water. After the gate

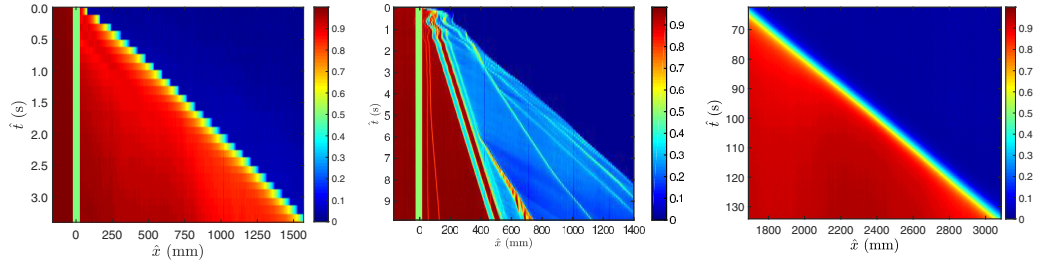

FIG. 3. Spatiotemporal diagrams of cross-sectional averaged concentration field, $\bar{C}_{\hat{y}}(\hat{x}, \hat{t})$, obtained from the same experiments as shown in Fig. 2. (a) Figure taken from Hasnain *et al.* [15]. (c) Figure taken from Alba *et al.* [16],

valve (pictured in green), is opened, the light fluid rapidly progresses downstream. The interface between the light and heavy fluids is smooth in the density-stable configuration, in contrast with the density-unstable configuration shown in Fig. 2(b), taken from Hasnain *et al.* [15]. In their computational study of miscible density-stable displacement flows in a plane channel, Etrati *et al.* [23] found that instabilities can form in the residual layer of the displaced fluid over time. Such instabilities may have been present in the current work but were not observed as a main feature of the flow. The notable differences between the density-stable and density-unstable cases are kinks and instabilities shown in Fig. 2(b). Through experimental and theoretical analyses, Hasnain *et al.* [15] showed that at early times there exist strong hydrodynamic shear instabilities in the form of Kelvin-Helmholtz mode, causing large amplitude waves. Such waves may coalesce and form sharp kinks that can further be triggered via surface-tension-driven Rayleigh instabilities at later times [Fig. 2(b)]. In Fig. 2(a) the light fluid in red leaves a barely visible layer of blue at the bottom, progressing forward above a thin layer of heavy fluid. This feature is common to all our density-stable experiments and is in contrast to the miscible density-stable case shown in Fig. 2(c) (taken from Alba *et al.* [16]), where the light fluid mixes with the heavy fluid at the bottom of the pipe instead of rising above it.

Figure 3 shows spatiotemporal diagrams of the cross-sectional-averaged concentration field, $\bar{C}_{\hat{y}}(\hat{x}, \hat{t})$, for the same experiments as in Fig. 2. The boundary between the light and heavy fluids in the immiscible density-stable case (current study) is clearly visible in Fig. 3(a). However, in the immiscible density-unstable case [15], there are a variety of waves and mixing bands obvious in Fig. 3(b) which correspond to hydrodynamic instabilities discussed in Fig. 2(b). The spatiotemporal diagram of the miscible density-stable case [16], given in Fig. 3(c), remains largely similar to that of immiscible case Fig. 3(a). However, as we will discuss throughout the rest of the paper, these flows can be significantly different in nature from one another.

Due to evident similarities in their flow patterns, we now focus on a comparison between immiscible and miscible density-stable flows. Figure 4(a) shows the experimental $\hat{h}/\hat{D}$ profiles at times $\hat{t} = [1.68, 1.96, 2.24, ..., 3.08, 3.36]$ s for an immiscible flow. We use $\hat{h}$ to represent the equivalent interface height; it is a function of downstream distance and time: $\hat{h}(\hat{x}, \hat{t})$. The normalized equivalent interface height, $\hat{h}/\hat{D}$, can be thought of as the shape of the interface between the heavy and light fluids. Marked differences from the miscible case [see Fig. 4(b)] can be observed. First, the top part of the flow section shows a sharper transition between the light and heavy fluid due to the absence of mixing. Second, it can be seen that the immiscible interface exhibits pinning behavior near the bottom of the pipe, where successive profiles extend farther and farther out from the same point close to the initial release, i.e., gate valve with $\hat{x} \approx 0$ mm. This is in contrast to the miscible case, where a profile looks almost identical to the previous and is simply shifted slightly downstream. The distance between subsequent profiles is referred to as the stretch length in the miscible case [16], but this parameter becomes ill-defined with immiscible fluids due to the pinning

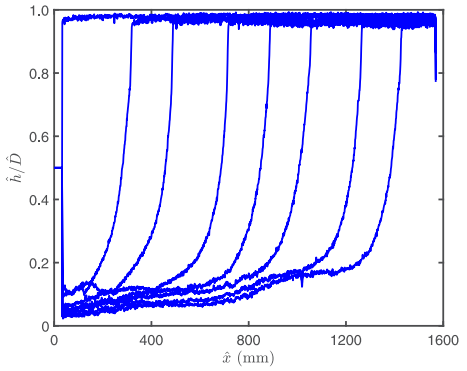

(a)

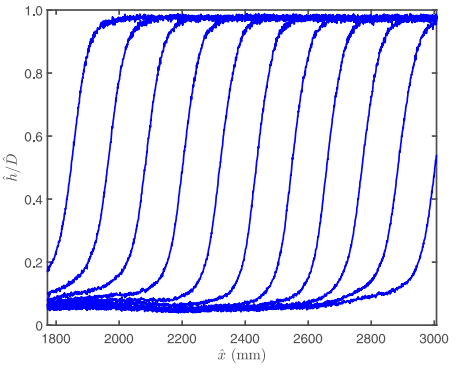

(b)

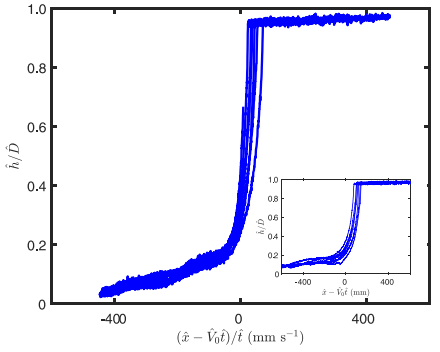

(c)

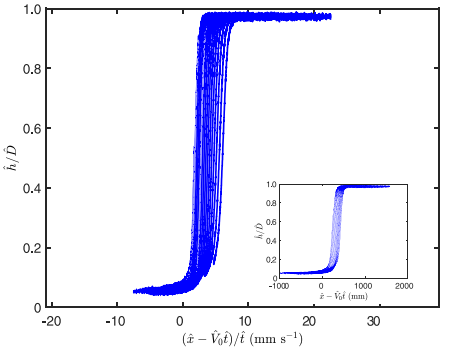

(d)

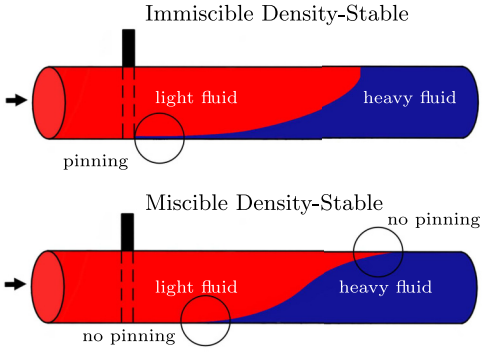

(e)

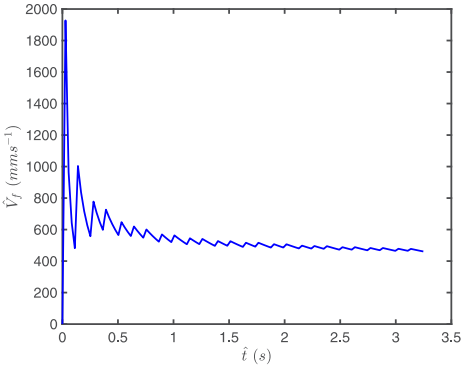

(f)

FIG. 4. (a) Experimental profiles of normalized $\hat{h}(\hat{x},\hat{t})$, at times $\hat{t} = [1.68, 1.96, 2.24,..., 3.08, 3.36]$ s and streamwise location, $\hat{x}$, for immiscible density-stable fluids, measured from the gate valve for the same experiment as shown in Fig. 2(a), where $\beta = 45^\circ$ and $\hat{V}_0 = 456.9\,\text{mm s}^{-1}$. (b) Experimental profiles of normalized $\hat{h}(\hat{x},\hat{t})$ at times $\hat{t} = [68, 74.5,..., 126.5, 133]$ s and streamwise location, $\hat{x}$, for miscible density-stable fluids (taken from Alba *et al.* [16]). (c) Normalized $\hat{h}(\hat{x},\hat{t})/\hat{D}$ profiles for the same experiment as Fig. 4(a) plotted against $(\hat{x}-\hat{V}_0\hat{t})/\hat{t}$. (Inset) $\hat{h}(\hat{x},\hat{t})/\hat{D}$ plotted against $(\hat{x}-\hat{V}_0\hat{t})$. (d) Collapse of the normalized $\hat{h}(\hat{x},\hat{t})/\hat{D}$ profiles with $(\hat{x}-\hat{V}_0\hat{t})/\hat{t}$ (taken from Alba *et al.* [16]). (Inset) $\hat{h}(\hat{x},\hat{t})/\hat{D}$ plotted against $(\hat{x}-\hat{V}_0\hat{t})$ (e) Schematic representation of pinning and nonpinning behavior in miscible and immiscible density-stable flows, respectively. (f) Experimental evolution of the displacing front velocity value $\hat{V}_f$ with time for the same density-stable experiment as in Fig. 4(a).

effect. For a steady-state flow, these profiles converge when plotted against $(\hat{x} - \hat{V}_0\hat{t})/\hat{t}$, as shown in Fig. 4(c) [24]. This similarity parameter represents placing the coordinate system at a point moving with speed $\hat{V}_0$. It also collapses all the profiles at various times, allowing for the comparison of experiments with different characteristics (e.g., density difference, At, angle, β, or velocity, $\hat{V}_0$) that fundamentally affect the instance it takes for each experiment to complete, i.e., front reaching the end of the pipe. This is particularly useful when we want to compare displacement efficiency for various cases. In the next section we will also compare against the choice of $\hat{x} - \hat{V}_0\hat{t}$ scaling parameter. Fig. 4(d) shows the experimental $\hat{h}/\hat{D}$ profiles for a miscible flow at times $\hat{t} = [68, 74.5,..., 126.5, 133]$ s, with the collapse of these curves against $(\hat{x} - \hat{V}_0\hat{t})/\hat{t}$ pictured in the inset. Notably, the interface shape and the distance between successive interfaces remain constant for the miscible case. This suggests that after an initial transitory phase, the leading and trailing fronts, the points farthest forward and farthest back in the interface, respectively, propagate forward at the same speed [16]. Note that the reason the profile limits do not exactly correspond to 0 and/or 1 in Fig. 4(b) is due to a measurement issue and not because of a residual film. In fact, this issue has been repeatedly reported and discussed in the literature [15,16,18,20]. Such measurement noise is due to the pipe wall and persists regardless of the use of a fish tank.

The pinning behavior indicates first that for immiscible fluids, the interface shape is continually stretching over time into a more elongated curve. It also indicates that there is a thin layer of heavy fluid remaining at the bottom of the pipe where the light fluid does not make contact with the base. In Fig. 4(a) it can be seen that two immiscible effects are in competition. First, the bulk influx of oil increasingly displaces the heavy fluid over time, causing the thin layer of heavy fluid to be reduced in height close to the gate area. Simultaneously, at the advancing front of the flow, the bottom edge of the interface is being increasingly sheared by the heavy fluid, causing the thin layer of heavy fluid to increase in height farther away from the gate area. This pinning behavior represents a significant departure from miscible density-stable flows, and is mainly considered to be due to the wetting and nonwetting nature of the fluids. In our current study, the heavy fluid is water densified with calcium chloride. The saltwater solution's greater ability to maintain contact with the surface of the pipe compared to the silicone oil results in a drag force on the oil that pins the interface to the gate region. In the miscible case, both fluids are equally wetting, allowing for the front to move smoothly along the bottom of the pipe after reaching a steady state. Note that in our experiments, we have found that the pinning effect does not strongly depend on the soap-cleaning procedure and/or surface tension value (see Fig. 10 below).

Fig. 4(e) shows a schematic representation of immiscible and miscible density-stable flows. The top inset shows that there is a thin layer of water at the bottom of the pipe in the immiscible case. The height of the thin layer is exaggerated for schematic purposes. The bottom inset for miscible flows illustrates the absence of pinning behavior, as the leading and trailing fronts are equally wetting. Fig. 4(f) shows a plot of $\hat{V}_f$ versus time, where $\hat{V}_f$ is the speed of the frontal region of displacement. From this chart, it can be seen that $\hat{V}_f$ reaches a steady-state value of 485 mm s^{-1} in the last half of the experiment. $\hat{V}_f$ is calculated in the same manner as the immiscible study by Hasnain *et al.* [15]: developed velocity values are compared in a large-scale perspective. The mean and standard deviation over the steady-state portion are taken to the be the average value and error in $\hat{V}_f$, respectively, and is what will be reported throughout the remainder of the paper. As discussed in Taghavi *et al.* [9], the efficiency of a displacement process (effectiveness in removing displaced fluid), ϵ, can be obtained from imposed and frontal velocities as $\epsilon = \hat{V}_0/\hat{V}_f$.

B. Effect of experiment variables on displacement efficiency

We now explore the effect of our experiment variables on $\hat{h}/\hat{D}$ profiles of the flow. The curvature of the averaged $\hat{h}/\hat{D}$ profiles gives an indication of the height of the thin layer of water beneath the advancing front of oil, as demonstrated in Fig. 5(a). The profile in this figure has a vertical straight-line interface that does not have much water beneath the oil, while Fig. 5(c) shows a more curved interface that has a greater height of water beneath the oil. This height is correlated to displacement

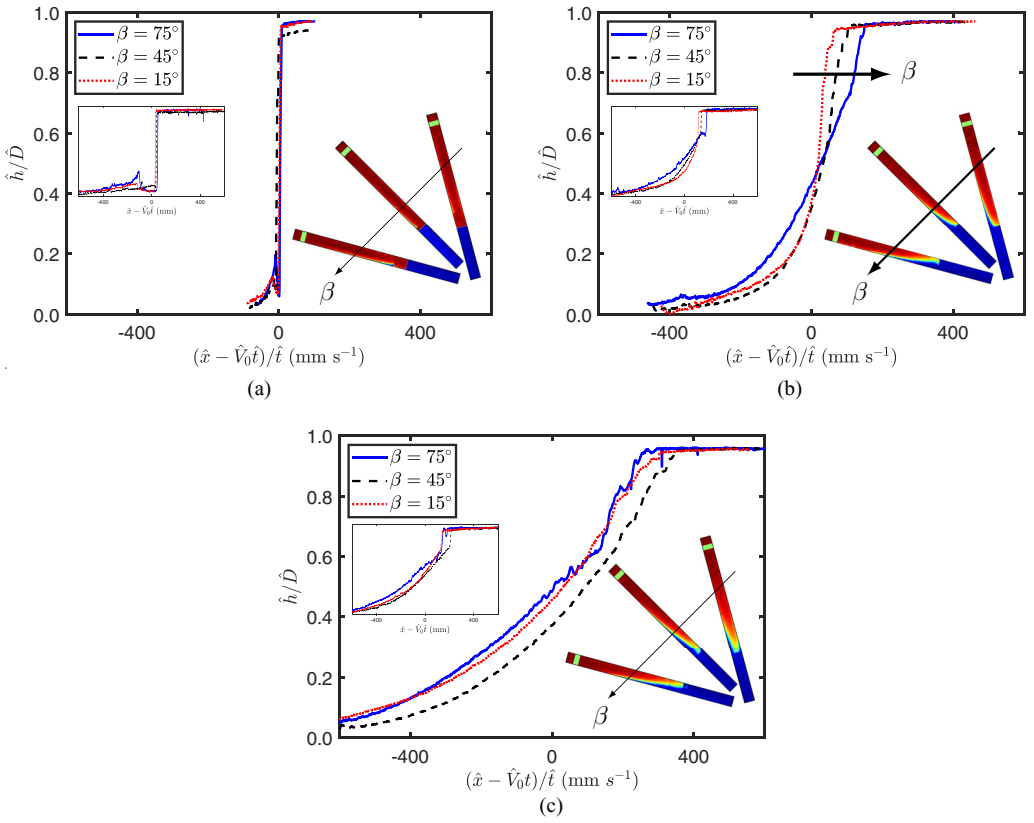

FIG. 5. Experimental profiles of $\hat{h}(\hat{x}, \hat{t})/\hat{D}$ for varying values of β with $\hat{\rho}_H = 998\,\text{kg m}^{-3}$ and $\hat{\rho}_L = 918\,\text{kg m}^{-3}$ (At $= -0.042$). (a) $\hat{V}_0 \approx 94$ mm s^{-1} (Re ≈ 172). (b) $\hat{V}_0 \approx 459$ mm s^{-1} (Re ≈ 838). (c) $\hat{V}_0 \approx 909$ mm s^{-1} (Re ≈ 1659). (Inset, left) $\hat{h}(\hat{x}, \hat{t})/\hat{D}$ plotted against similarity parameter $(\hat{x} - \hat{V}_0\hat{t})$. (Inset, right) Snapshots of the corresponding displacement flows.

efficiency, or the degree to which the displacing fluid evacuates the displaced fluid, because a larger height of water beneath the advancing displacing fluid means that less of the displaced fluid has been evacuated. As an inset to the figure, the $\hat{h}/\hat{D}$ profile is also plotted against similarity parameter $\hat{x} - \hat{V}_0\hat{t}$; this parameter does not use a scaling by time, and it is noted that flow features are strongly preserved in that presentation of the data as well. While $\hat{x} - \hat{V}_0\hat{t}$ requires the selection of different times (eg $\hat{t}_1$ and $\hat{t}_2$), at which two experiments reach the same $\hat{x}$ value, a more direct comparison (regardless of the instance in time) is possible with $(\hat{x} - \hat{V}_0\hat{t})/\hat{t}$.

Figure 5 plots averaged $\hat{h}/\hat{D}$ for varying values of β. In Fig. 5(a), experiments with low imposed velocities (Re < 600) are plotted. The resulting profiles are almost identical, indicating that at low Reynolds numbers, pipe inclination barely alters the flow. In other words, the efficiency of the displacement, which is related to the shape of the interface, remains the same with angle, β, at low imposed velocities. In Fig. 5(b) experiments with median imposed velocities ($600 <$ Re < 1500) are shown. In this region, a higher value of β results in a profile with more displaced fluid beneath the front. This indicates that at low β for this range of imposed velocities, a higher displacement efficiency is achieved. This variation in interface shape due to the pipe inclination can be understood by considering a sealed column of two fluids with different densities. The horizontal line that marks where the less dense fluid settles above the more dense fluid elongates when the column is horizontal compared to when it is vertical. Similarly, the interface between the light and heavy fluids in this

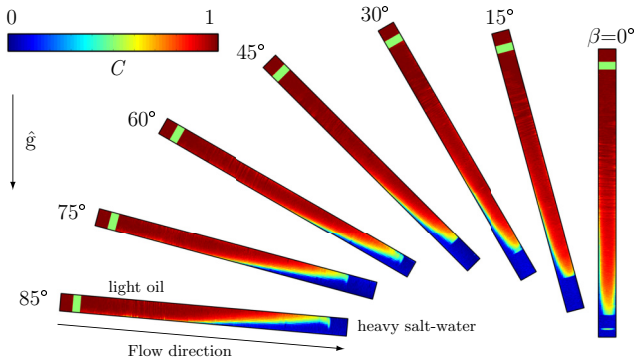

FIG. 6. Snapshots of change in isoviscous displacement flow with β for immiscible fluids in a density-stable configuration, obtained for $\hat{V}_0 \approx 475.8$ mm s^{-1}, $\hat{\rho}_H = 998$ kg m^{-3}, and $\hat{\rho}_L = 918$ kg m^{-3}, at time $\hat{t} \approx 2.5$ s. (At $= -0.042$, Re ≈ 868, Fr ≈ 7.61, Ca ≈ 0.68, $\theta = 56^\circ$) The field of view is 1659×9.53 mm^2. The color bar at the top left of the figure shows the corresponding concentration value, C, with 0 referring to the pure displaced fluid and 1 to the pure displacing fluid.

study is longer (covers a greater length of the pipe in the direction of the flow) at lower pipe tilt angles. Figure 5(c) shows that at the opposite extreme of Fig. 5(a), i.e., high imposed velocities (Re > 1500), a similar limit to the effect of β is reached. In this region, a change in inclination of the pipe also has little observable effect on the profile of the advancing front, although the curvature of the profile in this region is greatly increased compared to the curvature of the low Reynolds regime. This greatly increased curvature is thought to represent a limit of the flow after which the frontmost sections of the intruding oil begin to form a *ridge* feature which is described in further detail in Sec. III C.

Snapshots of the flow at a full range of pipe inclinations are shown in Fig. 6. It can be seen that in this regime of median Reynolds number, at lower pipe inclinations there is more displaced fluid pinned beneath the elongated advancing front, resulting in a lower displacement efficiency. This pattern is consistent across changes in density difference in our experimental range.

The effects of density variations on the shape of the interface between the two fluids is presented in Fig. 7(a) through changing Atwood number, At. Variations of the flow profile with At are similar to variations of the profile with the tilt angle β, in which a low Reynolds number (Re < 600) results in flow profiles that are flat and indistinguishable based on Atwood number [see Fig. 5(a)]. Results are not shown here for brevity. We have further confirmed that, at high Reynolds numbers as well, differences in Atwood number do not cause marked changes in flow profiles, although the profile once again adopts a more curved shape at Reynolds number greater than 1500 (results not shown). However, in the median Reynolds regime ($600 <$ Re < 1500), the effect of the Atwood number becomes clearer. Representative experiments in this regime are presented in Fig. 7(a), with corresponding snapshots provided in the inset. For similar imposed velocity ($\hat{V}_0 \approx 450.7$ mm s^{-1}) and the same pipe inclination $\beta = 60^\circ$, an increase in the density difference reduces the displaced fluid thickness beneath the advancing front, causing the interface to be flatter compared to a lower density difference. This behavior, which is in line with the findings of Alba *et al.* [16] for the miscible case, is due to the fact that there is a larger segregative force at the interface between the two fluids at higher |At|. As a result, in the median range of Reynolds number ($600 <$ Re < 1500), the interface elongation is reduced (higher displacement efficiency) as |At| is increased.

Variations of the flow profile with the imposed velocity, $\hat{V}_0$, are shown in Fig. 7(b). Among other controlling parameters, the imposed velocity was found to have the most prominent effect on the flow profile, causing variations from a flat interface shape at low $\hat{V}_0$ to a fully elongated front at high $\hat{V}_0$ consistently across all At and β values. These profiles had correspondingly lower and higher levels of heavy fluid beneath the front. Alba *et al.* [16] found that in a density-stable displacement

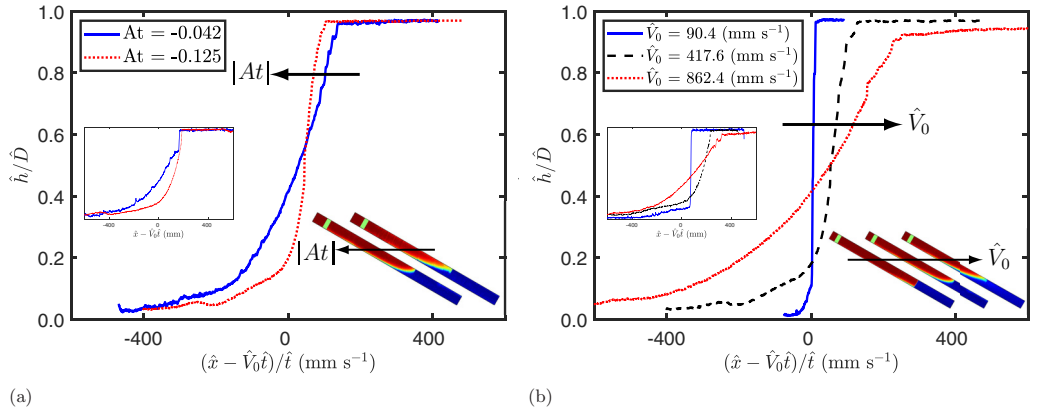

FIG. 7. Experimental profiles of $\hat{h}(\hat{x},\hat{t})/\hat{D}$, for varying values of (a) At and (b) $\hat{V}_0$ for $\beta = 60°$. Arrows indicate direction of increasing |At| and $\hat{V}_0$, respectively. (a) Similar $\hat{V}_0$ ($\hat{V}_0 \approx 450.7$ mm s^{-1}) and different At < 0 (Re ≈ 859, Fr $= [7.79, 3.86]$, Ca ≈ 0.64, $\theta = 56°$). (b) At $= -0.125$ with different $\hat{V}_0 = [90.4, 417.6, 862.4]$ mm s^{-1}(Re $= [181, 835, 1724]$, Fr $= [0.84, 7.79, 7.97]$, Ca $= [0.13, 0.69, 1.23]$, $\theta = 56°$). (Inset, left) $\hat{h}(\hat{x},\hat{t})/\hat{D}$ plotted against similarity parameter $(\hat{x} - \hat{V}_0\hat{t})$. (Inset, right) Snapshots of the corresponding displacement flows.

configuration, the interface stretching is controlled by the ratio of axial buoyancy forces to viscous stress, χ:

$$\chi = \frac{2\mathrm{Re}\cos\beta}{\mathrm{Fr}^2} = \frac{2\mathrm{At}\hat{g}\cos\beta\hat{D}^2}{\hat{\nu}\hat{V}_0} \tag{1}$$

As the imposed flow velocity, $\hat{V}_0$, is increased, $|\chi|$ is reduced, allowing the interface to spread more [Fig. 7(b)]. This finding can be of great importance in designing pipe displacement and cleaning processes, as low imposed velocities counterintuitively can result in a higher removal efficiency!

Figure 8 summarizes the effects of experiment variables on $\hat{V}_f$, the velocity of the displacing fluid front [15], over the full range of experiments. The dashed line is the linear fit $\hat{V}_f = 1.22\hat{V}_0$.

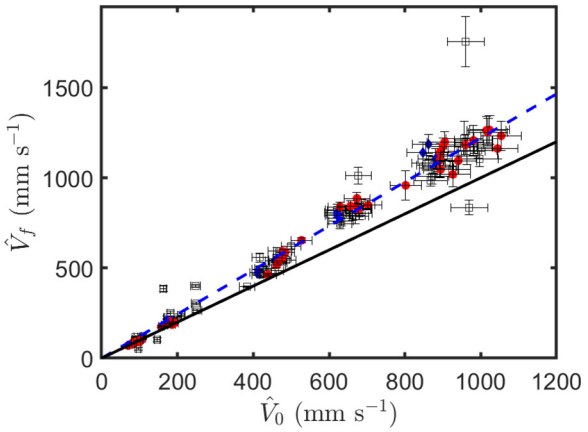

FIG. 8. Front velocity values, $\hat{V}_f$, plotted against the imposed flow velocity, $\hat{V}_0$, for the full range of experiments (At $= [-0.042$ (●), -0.075 (◆), -0.125 (□)], $\theta = [52, 56, 59]°$). The dashed line is the linear fit $\hat{V}_f = 1.22\hat{V}_0$. The solid line represents the ideal displacement case with $\hat{V}_f = \hat{V}_0$.

The displacement efficiency for these experiments is found to be $1/1.22 \approx 82\%$. This is a reduction of 14% from the miscible case, in which the displacement efficiency was found to be $\approx 96\%$ [16]. The lower values for immiscible experiments are likely due to the thin layer of displaced fluid that remains beneath the advancing front. Compared to the miscible case, the immiscible scenario demonstrates increased resistance to the forward motion of the incoming fluid, as the light oil is nonwetting while the heavy saltwater solution is wetting at the wall. At the contact point on the wall, the conflict due to wetting properties represents a region of friction and reduced flow speed relative to the incoming flow of oil. Accordingly, the flow pattern shows, most evidently at higher velocities, a faster-moving finger of oil advancing over a thin layer of slower-moving water (as opposed to a less-curved interface of oil-water progressing down the pipe with both fluids moving at a similar speed). The resulting flow pattern is less effective at evacuating the saltwater solution, leading to the loss in efficiency compared to the miscible case.

It should also be noted that for low imposed velocities $\hat{V}_0 < 300\,\text{mm s}^{-1}$ ($\text{Re} < 600$), the linear fit is $\hat{V}_f = 1.16\hat{V}_0$, which is closer to the ideal $\hat{V}_f = \hat{V}_0$ than the global fit, representing a displacement efficiency of $1/1.16 \approx 86\%$, or a 4% improvement over the combined set. As can be seen in Fig. 8, deviations of the ratio $\hat{V}_f/\hat{V}_0$ from the best fit line tend to grow larger as the mean imposed velocity $\hat{V}_0$ increases. This suggests that at larger Re, it is possible that due to these experimental fluctuations in the ratio $\hat{V}_f/\hat{V}_0$, a different value (slightly larger or less than 1.22) might be observed.

There exist a few theoretical works in the literature predicting the displacing front velocity, $V_f = \hat{V}_f/\hat{V}_0$ [9,25,26]. These papers mainly focus on density-unstable displacement flows at nearly horizontal configurations, assuming miscible fluids. Taghavi *et al.* [9] further discuss density-stable channel flows which represent the case of our paper more accurately (light displacing heavy). The values of the displacement front velocity, V_f, for the isoviscous case is given in the range 1.1–1.3 for $\chi = 2\text{Re}\cos\beta/\text{Fr}^2$ up to 10 (comparable to our experiments). The experiments carried out at nearly horizontal angle in our case correspond to $\beta = 75^\circ$ and 85°. We estimated the front velocity for these experiments and found out that $V_f \approx 1.19$, which is close to the values reported by Taghavi *et al.* [9]. The slight difference can be due to the immiscible effects as well as plane-channel versus pipe geometries adopted in the two studies.

C. Special features

During this study, the typical shape of the flow was that of an otherwise regular curve. However, typically at lower pipe inclinations and $\text{Re} > 600$, the shape of the advancing front formed an extended *ridge* shape. Figure 9(a) shows the development of such a ridge feature, while Fig. 9(b) plots the occurrence of the ridge's presence against dimensionless parameters. The dashed line in Fig. 9(b) plots the experimental fit:

$$\frac{\text{Re}\cos\beta}{\text{Fr}} = 0.15\text{Re} - 67. \tag{2}$$

This line splits the plane into regions without and with the ridge feature as well as regions with higher and lower displacement efficiencies (above and below the line, respectively). Displacement efficiency is defined as the volume of displaced fluid cleaned from the pipe after pumping the displacing liquid [9]. It can be calculated by taking the inverse of V_f, which is itself the mean imposed velocity $\hat{V}_0$ normalized by the parameter $\hat{V}_f$, i.e., $V_f = \hat{V}_f/\hat{V}_0$. When displacement efficiency ϵ is plotted against the dimensionless parameters above, ϵ varies most strongly with Re, decreasing as Re increases. Further, in the Re versus $\text{Re}\cos\beta/\text{Fr}$ plane, it is verified that the presence of the ridge feature often coincides with lower values of displacement efficiency (result not presented for brevity). This might be because, as can be seen in the last snapshot shown in Fig. 9(a), the longer the ridge extends, the more heavy fluid is held underneath the advancing front. Further, in a ridge formation the oil becomes more likely to break down into individual droplets that can separate from the main flow and cause a reduction in the displacing power of the bulk fluid.

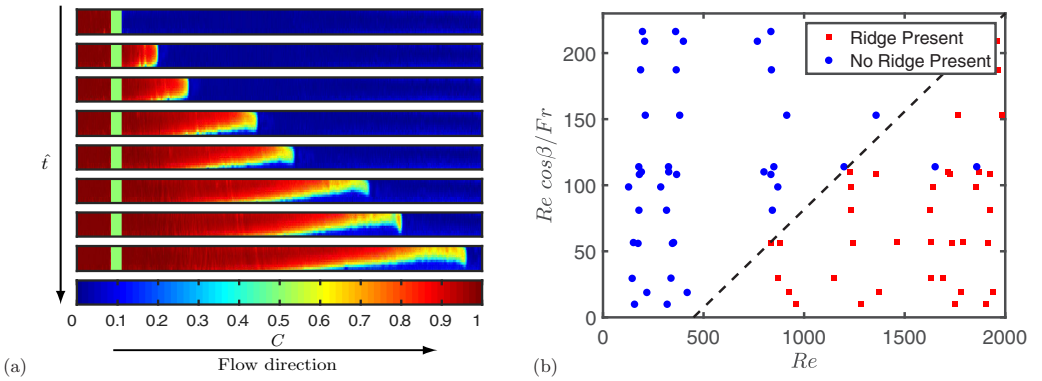

FIG. 9. (a) Experimental snapshots for $\beta = 60°$, $\hat{V}_0 = 893\,\text{mm s}^{-1}$, $\hat{\rho}_H = 998\,\text{kg m}^{-3}$, and $\hat{\rho}_L = 918\,\text{kg m}^{-3}$ at times $\hat{t} = [0.18, 0.36, 0.55, \ldots, 1.09]\,\text{s}$ ($\text{At} = -0.042$, $\text{Re} = 1629$, $\text{Fr} = 14.29$, $\text{Ca} = 1.28$, $\theta = 56°$), with a field of view of $1736 \times 9.53\ \text{mm}^2$. The bottommost image is a color bar of concentration C, with 0 and 1 referring to the displaced and displacing fluids respectively. (b) Full range of experiments ($\text{At} = [-0.042, -0.125]$, $\theta = 56°$), with the presence of a ridged feature marked with (■) and the absence of a ridged feature marked with (●). The dashed line marks $\text{Re}\cos\beta/\text{Fr} = 0.15\text{Re} - 67$, experimentally shown to divide between the presence and absence of a ridge feature.

D. Other water-oil solutions

The flow patterns described so far were observed for experiments with silicone oil as the displacing fluid. In order to evaluate the consistency of the reported experimental results when different viscosity values are employed, tests were also performed with other couples of immiscible fluids, using light viscosity ($\hat{\rho} = 853\ \text{kg m}^{-3}$, $\hat{\mu} = 0.018\ \text{Pa s}$, $\hat{\sigma} = 10.1\ \text{mN m}^{-1}$) and heavy viscosity mineral oils ($\hat{\rho} = 864\ \text{kg m}^{-3}$, $\hat{\mu} = 0.129\ \text{Pa s}$, $\hat{\sigma} = 33.4\ \text{mN m}^{-1}$) as the less dense displacing fluid. An additional 18 experiments were run to cover a broad range of inclination angle, β, and mean imposed velocity, $\hat{V}_0$, at density difference $\text{At} = -0.125$. The displaced saltwater solution was viscosified with xanthan gum in order to achieve an isoviscous experiment for silicone oil as well as light and heavy viscosity mineral oil (245, 450, 1170 mg liter^{-1}, respectively). Some viscosity differences did exist in the heavy mineral case. ($\hat{\mu}_H = 0.045\,\text{Pa s}$, $\hat{\mu}_L = 0.129\ \text{Pa s}$) The shear-thinning effects of xanthan gum are not significant in this range [15].

The results, presented in Fig. 10, show that in other oil-water flows, the same profile lengthening of the fluid interface occurs with the increase of inclination angle β. Pinning of the flow profile was also confirmed by the $\hat{h}/\hat{D}$ profiles of every oil-water solution tested (results not shown), with lower imposed velocities showing a more flat interface while higher $\hat{V}_0$ had more fluid held underneath the advancing front. It can further be observed in Fig. 10(a) that the front of the silicone oil interface protrudes further into the displacing fluid compared to the front of the light mineral oil [Fig. 10(b)], which is itself further than the front of the heavy mineral oil interface [Fig. 10(c)]. This is thought to be due to differences in surface tension $\hat{\sigma}$. As the surface tension decreases, the intruding oil is required to overcome less resistance in order to penetrate further into the fluid, and therefore silicone oil, the fluid with lowest surface tension, presents the most elongated shape of the three studied oils.

The best fit line for light mineral oil was $\hat{V}_f = 1.28\hat{V}_0$ compared to heavy mineral oil at $\hat{V}_f = 1.41\hat{V}_0$ and silicone oil $\hat{V}_f = 1.22\hat{V}_0$. Within each fluid pair tested, higher displacement efficiencies correspond with lower Re. Across the fluid pairs, the results suggest that the role immiscibility plays in the reduction of displacement efficiency is more pronounced with higher viscosity fluids.

E. UDV profile analysis

Ultrasonic Doppler velocimetry (UDV) provides insight into the internal dynamics of the flow by giving a view of the velocity profile in the vertical diametral plane. In Fig. 11 the results are

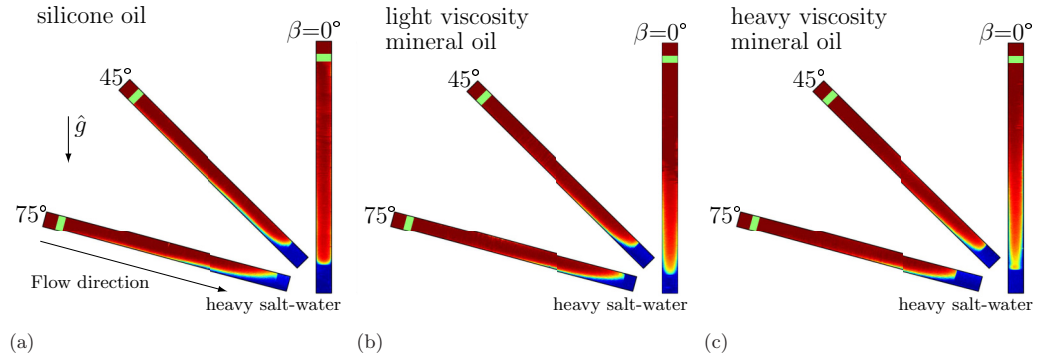

FIG. 10. Snapshots of change in isoviscous displacement flow with β for immiscible fluids in a density-stable configuration, obtained for At = 0.125. (a) Silicone oil displacing saltwater with $\hat{\rho}_H = 1181\,\mathrm{kg\ m^{-3}}$, $\hat{\rho}_L = 918\,\mathrm{kg\ m^{-3}}$, $\hat{\mu} = 0.005\,\mathrm{Pa\,s}$, $\hat{\sigma} = 3.5\,\mathrm{mN\ m^{-1}}$, and $\theta = 56^\circ$ (Re $\in$ [835, 914], Fr $\in$ [3.86, 4.22], Ca $\in$ [0.60, 0.65]). From left to right, $\hat{V}_0 = 417, 457, 418\,\mathrm{mm\ s^{-1}}$ and $\hat{t} = 1.3, 1.4, 1.4$ s. (b) Light viscosity mineral oil displacing saltwater with $\hat{\rho}_H = 1097\,\mathrm{kg\ m^{-3}}$, $\hat{\rho}_L = 853\,\mathrm{kg\ m^{-3}}$, $\hat{\mu} = 0.018\,\mathrm{Pa\,s}$, $\hat{\sigma} = 10.1\,\mathrm{mN\ m^{-1}}$, and $\theta = 52^\circ$ (Re $\in$ [220, 258], Fr $\in$ [3.94, 4.63], Ca $\in$ [0.76, 0.89]). From left to right, $\hat{V}_0 = 426, 487, 500\,\mathrm{mm\ s^{-1}}$ and $\hat{t} = 1.4, 1.2, 1.1$ s. (c) Heavy viscosity mineral oil displacing saltwater with $\hat{\rho}_H = 1110\,\mathrm{kg\ m^{-3}}$, $\hat{\rho}_L = 864\,\mathrm{kg\ m^{-3}}$, $\hat{\mu} = 0.129\,\mathrm{Pa\,s}$, $\hat{\sigma} = 33.4\,\mathrm{mN\ m^{-1}}$, and $\theta = 59^\circ$ (Re $\in$ [12, 18], Fr $\in$ [1.51, 2.30], Ca $\in$ [0.63, 0.96]). From left to right, $\hat{V}_0 = 249, 247, 162\,\mathrm{mm\ s^{-1}}$ and $\hat{t} = 1.1, 1.6, 1.7$ s. The field of view is $1903 \times 9.53\,\mathrm{mm^2}$.

presented for a median Reynolds experiment (Re = 853). Due to refraction errors, velocities at the far end of the pipe are difficult to measure, as reported in Alba *et al.* [18] and Hasnain *et al.* [15]. Guidelines are therefore provided to mark the shape of the flow. The probe captures profiles every 30 ms, and these profiles are averaged over ≈0.5 s, selected to achieve a balance of resolution fine enough to capture the flow features while reducing the effects of instantaneous variations in velocity.

Figure 11(a) presents snapshots of the flow over ≈2 s as it approaches and leaves the probe location, which is marked by the yellow line. The letters at the end of each snapshot correspond to the subfigure that displays the UDV profile at the probe location for that snapshot. At the beginning of the flow ($\hat{t} = [1.4, 1.9]$ s), only the heavy fluid is captured within the view of the probe, and the profile is shown to be fairly close to a rounded Poiseuille flow in Fig. 11(c). The moment at which the approaching oil front passes beneath the probe ($\hat{t} \approx 1.82$ s) is presented in Fig. 11(d). The flow is seen to be segmented into two distinct sections, with the top portion having a significantly accelerated velocity compared to the lower portion, which corresponds to regions of light oil and heavy saltwater, respectively. This emphasizes the fact that the light oil-based solution close to the upper wall of the pipe is *dragged* by the heavy water-based solution close to the bottom part of the pipe through interfacial viscous stress. The profile over the next 0.5 s ($\hat{t} = [1.9, 2.4]$) is presented in Fig. 11(e). The lower portion of the heavy saltwater region is again seen to be moving slower than the rest of the fluid, though to a lesser extent than before. Accordingly, the marked difference between the two regions of higher and lower velocity has been reduced, as more incoming oil adds momentum to the slower-moving lower portion. Figure 11(f) shows the profile averaged over the next 0.5 s ($\hat{t} = [2.4, 2.9]$), during which the fluid interface leaves the probe area. The remaining fluid is predominantly light oil, and the profile begins to approach a rounded Poiseuille profile once more.

IV. SUMMARY

The displacement flow of two immiscible isoviscous Newtonian fluids in an inclined pipe has been investigated experimentally in a density-stable configuration, where the nonwetting displacing

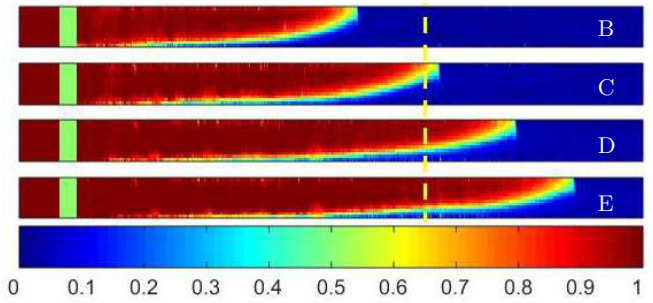

(a)

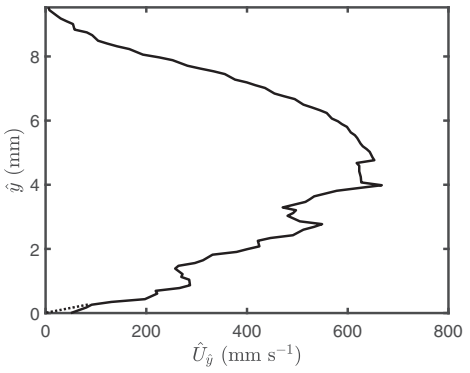

(b)

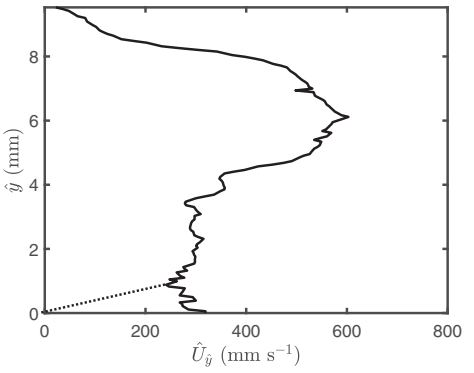

(c)

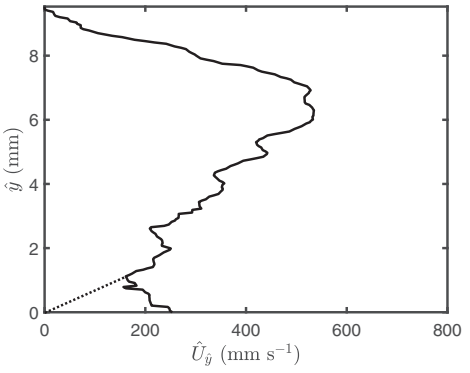

(d)

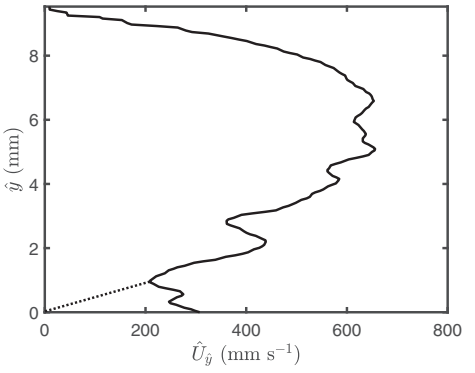

(e)

FIG. 11. (a) Experimental snapshots for $\beta = 75°$, $\hat{V}_0 = 426\,\text{mm s}^{-1}$, $\hat{\rho}_H = 1181\,\text{kg m}^{-3}$, and $\hat{\rho}_L = 918\,\text{kg m}^{-3}$ at different times $\hat{t} = [1.4, 1.9, 2.4, 2.9]$ s (At $= -0.125$, Re $= 853$, Fr $= 3.94$, Ca $= 0.61$, $\theta = 56°$). The field of view is $1692 \times 9.53\,\text{mm}^2$. The bottommost image is a color bar of concentration C, with 0 and 1 referring to the displaced and displaced fluids, respectively. Each snapshot is assigned a letter B to E. The representative UDV profiles to these flows are plotted in panels (b) to (e). (b) Velocity profile averaged over $\hat{t} = [1.4, 1.9]$ s, when only the displaced densified water flows under the UDV probe. (c) Velocity profile at $\hat{t} \approx 1.82$ s, the moment at which the front arrives at the probe. (d) Velocity profile averaged over $\hat{t} = [1.9, 2.4]$ s, as the interface leaves the probe area. (*e*) Velocity profile averaged over $\hat{t} = [2.4, 2.9]$ s, when displacing oil has begun to dominate the flow profile. The dotted lines in panels (b) to (e) for $\hat{y} \lesssim 1$ are guides to the eye correcting the UDV refraction errors close to the lower wall.

fluid is less dense than the wetting displaced fluid. Our experiments have covered a broad range of governing dimensionless parameters (Re, β, At). In contrast to the immiscible density-unstable case, the flow pattern was smooth, without characteristic interfacial instabilities. *Pinning* characteristics were observed in the immiscible density-stable flow and not the miscible density-stable flow. The displacement efficiency, as quantified by the ratio $\hat{V}_0/\hat{V}_f$, was found to be greater at low Reynolds and lower at high Reynolds numbers. This is a departure from the consistent linear fit described in the miscible case. Overall, a displacement efficiency of $\approx 82\%$ was found in immiscible density-stable flows, a decrease of 14% from the $\approx 96\%$ efficiency of the miscible case. This reduction of displacement efficiency in the immiscible case is attributed to wetting and nonwetting properties of the fluids. We highly anticipate the displacement efficiency to increase (even more so than the miscible case) if a wetting fluid displaces a nonwetting one.

The flow was found to be governed largely by Reynolds number. However, within the median Reynolds regime ($500 < \mathrm{Re} < 1500$), increased pipe inclination and increased density difference were found to increase the displacement efficiency. The effects observed in immiscible displacement flows using silicone oil-water solutions were found to persist for other mineral oil-water mixtures as well. Ultrasonic Doppler velocimetry was used to better understand the internal workings of the flow, and a segmented velocity profile was observed at the location of the interface. A ridge feature was observed in the flow and its presence was linked to a lower displacement efficiency. Future experimental work on immiscible density-stable displacement flows will focus on examining non-Newtonian shear-thinning and viscoplastic effects as well as wetting and nonwetting properties in these flows.

ACKNOWLEDGMENTS

This research has been conducted at the University of Houston, using the startup fund of K.A., supported financially by the National Research University Fund (NRUF). We would like to thank the reviewers for their helpful comments. Leontios Leonidu and Ali Khodaee are sincerely thanked for assisting in running the experiments.

[1] M. Fan, D. M. Phinney, and D. R. Heldman, Effectiveness of rinse water during in-place cleaning of stainless steel pipe lines, J. Food. Sci. **80**, E1490 (2015).

[2] M. J. Lehtola, T. K. Nissinen, I. T. Miettinen, P. J. Martikainen, and T. Vartiainen, Removal of soft deposits from the distribution system improves the drinking water quality, Water Res. **38**, 601 (2004).

[3] B. Shu, S. Zhang, and M. Liang, Estimation of the maximum allowable drilling mud pressure for a horizontal directional drilling borehole in fractured rock mass, Tunnelling, Underground Space Technol. **72**, 64 (2018).

[4] V. Hilton, A. Sapru, and M. Pavlovic, Detailed reservoir characterization utilizing oil-based micro-resistivity image logs, Society of Petrophysicists, and Well-Log Analysts, June 2003.

[5] R. J. Laronga and E. Shalaby, Borehole imaging technology visualizes photorealistically in oil-based muds, J. Pet. Technol. **66**, 36 (2014).

[6] T. Séon, J.-P. Hulin, D. Salin, B. Perrin, and E. J. Hinch, Buoyant mixing of miscible fluids in tilted tubes, Phys. Fluids **16**, L103 (2004).

[7] T. Séon, J. Znaien, D. Salin, J. P. Hulin, E. J. Hinch, and B. Perrin, Transient buoyancy-driven front dynamics in nearly horizontal tubes, Phys. Fluids **19**, 123603 (2007).

[8] S. Taghavi, K. Alba, T. Seon, K. Wielage-Burchard, D. M. Martinez, and I. Frigaard, Miscible displacement flows in near-horizontal ducts at low Atwood number, J. Fluid Mech. **696**, 175 (2012).

[9] S. M. Taghavi, T. Seon, D. M. Martinez, and I. A. Frigaard, Buoyancy-dominated displacement flows in near-horizontal channels: The viscous limit, J. Fluid Mech. **639**, 1 (2009).

[10] P. Petitjeans and T. Maxworthy, Miscible displacements in capillary tubes. Part 1. Experiments, J. Fluid Mech. **326**, 37 (1996).
[11] R. Balasubramaniam, N. Rashidnia, T. Maxworthy, and J. Kuang, Instability of miscible interfaces in a cylindrical tube, Phys. Fluids **17**, 052103 (2005).
[12] E. Lajeunesse, J. Martin, N. Rakotomalala, D. Salin, and Y. C. Yortsos, Miscible displacement in a Hele-Shaw cell at high rates, J. Fluid Mech. **398**, 299 (1999).
[13] J. Kuang, T. Maxworthy, and P. Petitjeans, Miscible displacements between silicone oils in capillary tubes, Eur. J. Mech. B **22**, 271 (2003).
[14] S. M. Taghavi, T. Séon, D. M. Martinez, and I. A. Frigaard, Influence of an imposed flow on the stability of a gravity current in a near horizontal duct, Phys. Fluids **22**, 031702 (2010).
[15] A. Hasnain, E. Segura, and K. Alba, Buoyant displacement flow of immiscible fluids in inclined pipes, J. Fluid Mech. **824**, 661 (2017).
[16] K. Alba, S. M. Taghavi, and I. A. Frigaard, Miscible density-stable displacement flows in inclined tube, Phys. Fluids **24**, 123102 (2012).
[17] D. F. Swinehart, The Beer-Lambert law, J. Chem. Educ. **39**, 333 (1962).
[18] K. Alba, S. M. Taghavi, and I. A. Frigaard, Miscible density-unstable displacement flows in inclined tube, Phys. Fluids **25**, 067101 (2013).
[19] A. Etrati, K. Alba, and I. A. Frigaard, Two-layer displacement flow of miscible fluids with viscosity ratio: Experiments, Phys. Fluids **30**, 052103 (2018).
[20] B. Eslami, S. Shariatnia, H. Ghasemi, and K. Alba, Non-isothermal buoyancy-driven exchange flows in inclined pipes, Phys. Fluids **29**, 062108 (2017).
[21] N. Mirzaeian and K. Alba, Monodisperse particle-laden exchange flows in a vertical duct, J. Fluid Mech. **847**, 134 (2018).
[22] M. Nowak, Wall shear stress measurement in a turbulent pipe flow using ultrasound doppler velocimetry, Exp. Fluids **33**, 249 (2002).
[23] A. Etrati, E. Stuart, K. Alba, M. Taghavi, and I. Frigaard, Miscible density-stable displacement flow in incline channels, 22nd Annual Conference of the CFD Society of Canada, June 2014.
[24] A. Hasnain and K. Alba, Buoyant displacement flow of immiscible fluids in inclined ducts: A theoretical approach, Phys. Fluids **29**, 052102 (2017).
[25] S. M. Taghavi, T. Séon, K. Wielage-Burchard, D. M. Martinez, and I. A. Frigaard, Stationary residual layers in buoyant Newtonian displacement flows, Phys. Fluids **23**, 044105 (2011).
[26] M. Moyers-Gonzalez, K. Alba, S. M. Taghavi, and I. A. Frigaard, A semi-analytical closure approximation for pipe flows of two Herschel-Bulkley fluids with a stratified interface, J. Non-Newtonian Fluid Mech. **193**, 49 (2013).